A&A 437, 599–609 (2005)
DOI: 10.1051/0004-6361:20052650
© ESO 2005

Astronomy & Astrophysics

XMM-Newton observations of β Centauri (B1 III): The temperature structure in the hot plasma and the photosphere-wind connection

A. J. J. Raassen[1,2], J. P. Cassinelli[3], N. A. Miller[4], R. Mewe[1], and E. Tepedelenlioğlu[5]

[1] SRON National Institute for Space Research, Sorbonnelaan 2, 3584 CA Utrecht, The Netherlands
e-mail: a.j.j.raassen@sron.nl
[2] Astronomical Institute "Anton Pannekoek", Kruislaan 403, 1098 SJ Amsterdam, The Netherlands
[3] Dept. of Astronomy, University of Wisconsin at Madison, 6251 Sterling Hall, North Charter Str., Madison, WI 53706, USA
[4] Dept. of Physics & Astronomy, University of Wisconsin-Eau Claire, 105 Garfield Avenue, Eau Claire WI 54702, USA
[5] Physics Deparment, University of Wisconsin-Madison, 1150 University Ave., Madison, WI 53706, USA

Received 6 January 2005 / Accepted 16 March 2005

Abstract. We present *XMM-Newton* observations of the B giant β Centauri (B1 III). The spectra are rich of spectral lines from a wide range of ionization stages which indicate temperatures in the range ~0.1−0.6 keV. Simultaneous fits to the RGS, EPIC-MOS, and EPIC-pn spectra yield three plasma temperatures (0.1, 0.2, and 0.6 keV), emission measures, and elemental abundances which are quite close to solar values. These temperatures are confirmed by DEM modeling. According to the derived models the intrinsic source X-ray luminosity in the energy range 0.3−10 keV is $L_x = 10 \times 10^{30}$ erg s^{-1} at a distance of 161 pc. An analysis of the X-ray light curve suggests that the photospheric variability does not have much of an effect on the properties of the X-ray luminosity. The sensitivity of the He-like forbidden and intercombination lines to a strong ultraviolet stellar radiation field is used to constrain the radial distances at which the lines of Ne IX, O VII, and N VI originate.

Key words. stars: early-type – stars: winds, outflows – stars: variables: β Cephei

1. Introduction

The star β Centauri is a giant of spectral type B1 III. Its *Hipparcos* distance $d = 161$ pc (Perryman et al. 1997), its column density $N_H = 4.27 \times 10^{19}$ cm^{-2} (Fruscione et al. 1994), and its effective temperature $T_{eff} = 21\,100$ K (Flower 1977). The *Einstein* X-ray survey (Grillo et al. 1992) has shown that X-ray luminosities $L_x \gtrsim 10^{30}$ erg s^{-1} are quite common in B stars of early spectral type B0-3, regardless of luminosity class, but that X-ray emission becomes weaker or nonexistent in later B-type stars.

β Cephei variables are a small group of short-period pulsating variables lying slightly above the upper main sequence. They are confined within a narrow band of the H-R diagram which lies near the end of core hydrogen-burning stars of roughly 10−20 $M_\odot$ and many of them have a doubly periodic light curve (a short and a long period). The same is true for β Cen (Breger 1967)

Although it is a β Cephei variable, the other properties of β Cen are typical for other B stars, as was found in the study of β Cephei stars by Agrawal et al. (1984). Thus its global, time-averaged properties will shed light on the X-rays from all hot stars. The B stars have been the source of numerous surprises during the past decade of high energy astronomy.

In the present paper the measurements with *XMM*-EPIC and -RGS are fitted with multi-temperature optically thin models in collisional ionization equilibrium (CIE) to derive the distribution of emission measure versus temperature and to obtain elemental abundances. We present an analysis of the spectral lines, including several that have not been studied earlier (e.g., lines from N VII and C VI).

2. Observations

A log of our *XMM-Newton* observations of β Cen is shown in Table 1. For information on *XMM-Newton* and its X-ray instruments, i.e. the European Photon Imaging Cameras (EPIC) MOS and pn and high-resolution Reflection Grating Spectrometers (RGS) we refer to the publications by den Herder et al. (2001), Jansen et al. (2001), Strüder et al. (2001), and Turner et al. (2001).

The data have been reduced with standard procedures using the *XMM-Newton* Science Analysis System (SAS version 5.4.1) with the calibration data available in June 2001. The EPIC response matrices that have been used to fit the CCD spectra have been constructed by extraction using rmfgen and arfgen tools. The RGS1 and RGS2 spectra have been co-added. The spectra are shown in Fig. 1. The spectra are dominated

Article published by EDP Sciences and available at http://www.edpsciences.org/aa or http://dx.doi.org/10.1051/0004-6361:20052650

Table 1. Observation log of the data of β Cen.

Instr.	Filter	Mode	Date-obs-start	Date-obs-end	Duration(s)
MOS1	Thick	Full Frame	2003-07-19T07:48:05	2003-07-20T00:25:04	59 639
MOS2	Thick	Full Frame	2003-07-19T07:48:10	2003-07-20T00:25:09	59 639
pn	Thick	Full Frame	2003-07-19T08:22:15	2003-07-20T00:25:24	57 319
RGS1	None	Spec+Q	2003-07-19T06:09:52	2003-07-20T00:26:19	65 685
RGS2	None	Spec+Q	2003-07-19T06:09:52	2003-07-20T00:26:19	65 685

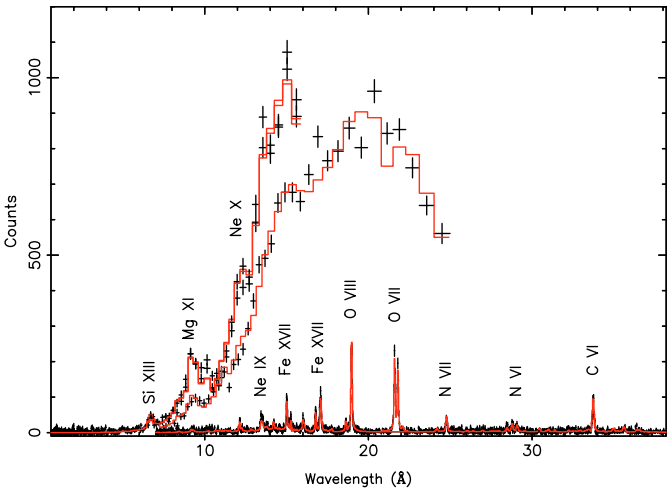

Fig. 1. Background-subtracted EPIC-MOS (*upper curve*), EPIC-pn, and first-order RGS spectra of β Cen. Error bars indicate 1σ statistical errors including the effect of background. The unbroken (red in the electronic version) curve shows the best-fit model (cf. Table 2). A number of prominent lines are labelled with the emitting ions. Due to the pile-up and the use of an annulus to extract the spectrum EPIC-pn has less counts than EPIC-MOS..

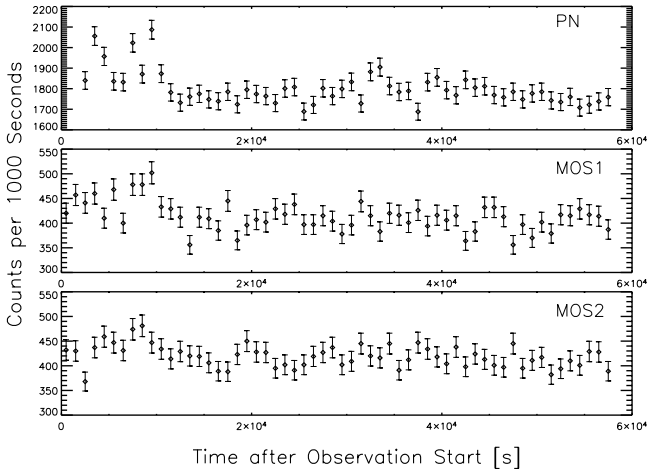

Fig. 2. Background-subtracted light curves of β Cen created from data taken with the pn (*top*), MOS1 (*middle*), and MOS2 (*bottom*), binned in 1000-s intervals.

by the H- and He-like ions of the elements Si, Mg, Ne, O, N, and C, along with Fe XVII lines. The pn data suffered some pile-up. Therefore an annulus was used to extract the spectrum. This diminished the number of counts in the pn spectrum.

3. Light curve analysis

Observations with *EUVE* showed that β CMa displays periodic variability in its Lyman continuum on the same time scale as its optical and UV variability (Cassinelli et al. 1996). There have also been reports that the X-ray flux of the β Cephei stars varies on the same period as the optical and UV photospheric continua (Cohen et al. 1996). Thus such stars are very important for unraveling the "wind-photosphere" connection in hot stars (Kaper 1999; Kaper et al. 1999). There is a growing realization that modulations in wind properties are related to photospheric variability. In this paper, we investigate search for changes in the temperature of the X-ray source and the ionization balance in the wind of β Cen.

β Centauri (HD 122451) is a β Cephei variable with a pulsation period of 0.157 day (Sterken & Jerzykiewicz 1993), typical for members of that class (Lesh & Aizenman 1978). During our *XMM* observations it undergoes about 4 optical pulsation cycles. In addition to this star's X-ray spectrum, its light curve should be particularly interesting. In general hot star X-ray fluxes are relatively constant in time, and generally do not show periodic variations. However, in this case it is important to note that β Cen is a β Cephei variable, indicating that the physical conditions at the base of the wind are being modulated in a periodic fashion. If that same region is an important contributor to the star's overall X-ray flux, it is natural to assume that there may be a corresponding modulation of β Cen's X-ray output.

For this observation, the RGS data are not very useful for light curve analysis because of the low count rate. However, because of the minimal problems with pileup for point sources for XMM detectors, the three direct-image EPIC detectors can be used to produce very useful light curves. A first look at the background-subtracted light curves (Fig. 2) does not show any obvious periodic modulation in any of the three EPIC detectors. A slight "flare" is apparent near the beginning of the observation, quite pronounced in the pn data, but only faintly visible in the two MOS light curves. This is somewhat puzzling because the energy response curves of the pn and MOS instruments are not that different from one another, with the pn having an only slightly harder response (see XMM UHB 3.2.2.1)[1].

To investigate this issue in more detail, the MOS counts were divided into three energy bands (0.3−0.9 keV, 0.9−2.7 keV, and 2.7−8.1 keV), and six separate MOS light

[1] Effective Areas: 3.2.2.1
`http://heasarc.gsfc.nasa.gov/docs/xmm/uhb/node20.html`

curves were constructed, one for each of the two detectors in each of the three energy bands. Upon inspection, it was apparent that the "flare" seen in the pn data was also clearly present in the MOS data, but only in the highest energy band. This behavior indicates that this event seen in our data is probably one of the the soft proton-induced "flares" seen in some XMM datasets. These are most likely caused by the passage of the satellite through proton clouds in the Earth's magnetosphere (see XMM UHB 3.3.7.1)[2]. In order to remove the effects of the flare-contaminated interval, we discarded the first 12 ks of this observation for the purposes of the light curve analysis described below. It should be noted that this segment of the observation is still used in the analysis of the RGS data, because the order-sorting routines used in RGS data analysis mean that this background can have only a negligible effect on the extracted RGS spectra.

Though the low count rates inherent in X-ray data make a general search for low amplitude periodic variability difficult, in the case of β Cephei stars such as β Cen, we are aided by being primarily interested in X-ray variation on the period of the star's optical variation. For this data set, we are particularly interested in any modulation of the X-ray output on the photospheric pulsational time scale of 0.157 day (Sterken & Jerzykiewicz 1993). To see if there is any variation of the X-ray flux on that time scale, we folded the X-ray light curve on that period. The data were folded using time bins ranging from 100 s to 3000 s. In this manner we looked at the pn data, the two MOS data sets separately and jointly, and the MOS data divided into the soft, medium, and hard bands described above. In each case, no simple modulation on the photospheric period was apparent.

The folded light curves for the pn and the MOS1+MOS2 data are displayed in Fig. 3 binned in 1000 s intervals (a convenient binning because the 0.157 day period = 13.6 ks, giving us roughly 13 sample points over each period).

As a general test for cyclic variability, we constructed Scargle periodograms for the various data sets described above (pn, MOS individual, MOS combined, MOS divided into three energy bands) in various binnings. In each case, no periodicities with high statistical confidence were found. There was no hint of periodicity on the optical period even considering periodogram peaks with low statistical confidence.

As a final note, it is interesting to compare the light curves with the constant source hypothesis. Using only the data occurring after the background flaring region, the reduced χ^2 for the pn data is 1.186, while that of the combined MOS data is 0.977. These correspond to probabilities of 83% and 49% (respectively) that the source is not fully consistent with a constant source. This indicates that there is some, though very small, variability in excess of that expected from a constant source. It should also be kept in mind that some variability in excess of that expected through counting statistics could be attributed to the combination pixel-to-pixel gain variation and satellite dither.

[2] Soft Proton Flares:
http://heasarc.gsfc.nasa.gov/docs/xmm/uhb/node34.html

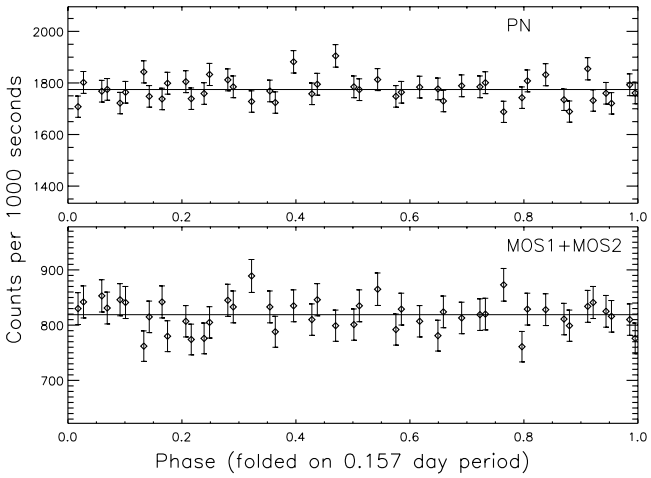

Fig. 3. The X-ray light curve of β Cen binned in 1000-s intervals and folded on the 0.157 day optical period. The top panel gives the light curve for the pn detector, while the bottom panel is the added count rates of the two MOS detectors to achieve a better signal strength. The horizontal lines indicate the average count rates for these instruments during our observation. The zero point for the phasing is taken to be where the flare-contaminated data ends.

In summary, the fact that β Cen is a β Cephei variable does not seem to have much of an effect on the properties of its X-ray light curve, and that this source is basically consistent with the general lack of short-term X-ray variability seen for OB stars in general.

4. Spectral analysis

The *XMM* observations enable us also to carry out an analysis of the line spectrum. This can provide clues regarding the nature of the X-ray sources in the outer atmosphere and wind of β Cen. We start with an analysis of the source temperature(s) in this star.

4.1. Multi-temperature fitting

4.1.1. A 3 temperature collisional ionization equilibrium model

We have determined the thermal structure and the elemental composition of β Cen's X-ray emitting plasma by means of multi-temperature fitting to the spectrum, as follows: we fitted multi-T optically thin plasma models (i.e., collisional ionization equilibrium (CIE)) of the combined spectra of the EPIC-MOS and -pn and the RGS using our spectral analysis program SPEX (Kaastra et al. 1996a) in combination with the MEKAL (Mewe-Kaastra-Liedahl) optically thin plasma code as developed by Mewe et al. (1985, 1995). The MEKAL data base is given as an extended list of fluxes of more than 5400 spectral lines, and is available on the web[3].

In the multi-temperature calculations we used three temperatures which were automatically found by the fitting procedure. The three temperature components were coupled to

[3] http://www.sron.nl/divisions/hea/spex/version1.10/line/

one $N_{\rm H}$ absorption column density, related to the interstellar medium (ISM), and one set of abundances. The temperature components, emission measures and abundances were free to vary. The assumed column density (Fruscione et al. 1994), and the derived temperatures, emission measures $EM = \int n_{\rm e} n_{\rm H} {\rm d}V$, luminosities, and elemental abundances are given in Table 2, together with the statistical $1\,\sigma$ uncertainties. The column density, $N_{\rm H}$, takes into account absorption by the interstellar medium. We considered the possible absorption within the wind and found there was no need to introduce additional absorption to account for stellar wind effects. The three temperatures stretch over a wide range, peaking at 0.08, 0.21, and 0.59 keV i.e., at 0.9, 2.4, and 6.8 MK. Due to the observed lines being narrow (i.e., only 1.4 times the instrumental width) the fitted values of the velocities $v_{\rm mic}$ are low and not very robust. Fixing the $v_{\rm mic}$ of the cool component (T_1) to the average value of the medium and hot components worsens the fit results. The $v_{\rm mic}$ of the cool component is only affected by the lines of N VI and C VI. Therefore, this value is determined by fitting in a limited wavelength range (27−35 Å), while the other parameters were fixed. Table 2 also presents the X-ray luminosity in the XMM (0.3−10 keV) band, which is the intrinsic model luminosity at the place of the emitting plasma, i.e., corrected for absorption by the interstellar medium (ISM). If we scale the model X-ray luminosity to the *ROSAT* band (0.1−2.5 keV) we obtain a value of 15 (in units of 10^{30} erg s^{-1}), comparable to the value of 20 Cassinelli et al. (1994) found from *ROSAT* observations. For the purposes of comparison we have adjusted their reported flux measurement to compensate for the fact that they assumed a distance of 85 pc instead of the 161 pc value adopted here. It is also similar to the *Einstein* value of 13 for the band 0.15−4 keV (Grillo et al. 1992). But their flux measurement has also been scaled to a distance of 161 pc from their assumed distance of 110 pc. The results of the 3-T fit are shown in Fig. 1. The points with error bars are the data. The unbroken curve (red in the electronic version) is the best fit model.

Table 2. Multi-temperature fitting for *XMM* combined EPIC-pn, -MOS & RGS spectra of β Cen[a].

comp. i	1	2	3
$N_{\rm Hi}$[b]	4.27	4.27	4.27
$kT_{\rm i}$[c]	0.076 ± 0.036	0.208 ± 0.032	0.587 ± 0.069
$EM_{\rm i}$[d]	6.51 ± 1.33	2.35 ± 0.08	1.39 ± 0.03
$L_{\rm xi}$[e]	1.87	4.59	3.81
$v_{\rm mic}$[f]	532 ± 108	280 ± 110	230^{+150}_{-230}
$\sum_{\rm i} L_{\rm xi}$[e]		10.3	
Abun.[g]			
C	0.98 ± 0.06		
N	1.17 ± 0.10		
O	1.04 ± 0.03		
Ne	1.23 ± 0.08		
Mg	1.59 ± 0.09		
Si	1.05 ± 0.13		
S	0.55 ± 0.12		
Ar	1		
Ca	1		
Fe	1.13 ± 0.02		
Ni	1		
$\chi^2_{\rm red}$	2594/2031		

Notes:
[a] *HIPPARCOS* distance d = 161 pc is used.
[b] Column density (10^{19} cm^{-2}) assumed.
[c] Temperature in keV.
[d] Emission measure in 10^{53} cm^{-3}.
[e] X-ray luminosity (0.3–10 keV) in 10^{30} erg s^{-1}.
[f] Microturbulent velocity (in km s^{-1}) representing line broadening.
[g] Abundance relative to solar photospheric number abundance (Anders & Grevesse 1989 with Grevesse & Sauval 1998, 1999 for Fe).

4.1.2. Abundance determination

The abundances given in Table 2, are relative to solar photospheric values from optical studies (Anders & Grevesse 1989) except for Fe, for which we use $\log A_{\rm Fe} = 7.50$ (see Grevesse & Sauval 1998 and 1999) instead of 7.67 (Anders & Grevesse 1989). Here $\log A_{\rm Fe}$ is the logarithm of the Fe-abundance relative to $\log A_{\rm H} = 12.0$. From cool stars it is known that the hot X-ray emitting plasma (the corona) show abundances that differ from the photospheric abundances. For the Sun Feldman (1992) established a First Ionization Potential (FIP) effect. This implies that the elements with a low first ionization potential, such as Fe, Mg, Si are enhanced in the corona. The same effect was also observed in other cool stars (Raassen et al. 2003). The opposite was found in very active cool stars (Audard et al. 2003). This is called the Inverse FIP effect. In β Cen we obtain solar photospheric abundance values for the X-ray spectrum. Comparison with solar values is a bit artificial, but needed due to the lack of stellar photospheric abundances. So no prominent abundance peculiarity is determined.

4.1.3. DEM modeling

Apart from a multi-T fitting, the combined EPIC-MOS and RGS spectrum was also fitted by means of a differential emission measure (DEM) model (e.g., Kaastra et al. 1996b) using the module "pdem" in SPEX. This module, which is based on a spectral description by means of a spline-method offers the possibility to obtain the differential emission measure distribution and the abundances simultaneously and for different $N_{\rm H}$ values.

We define the DEM by $n_{\rm e} n_{\rm H} {\rm d}V/{\rm d}\log T$ (integrated over one logarithmic temperature bin). The result for the EM (per logarithmic temperature bin) is shown in Fig. 4. The temperature structure obtained using the DEM-modeling covers the same temperature range as the 3-T fit. Here we determine a continuous temperature distribution, peaking at the temperatures given in Table 2.

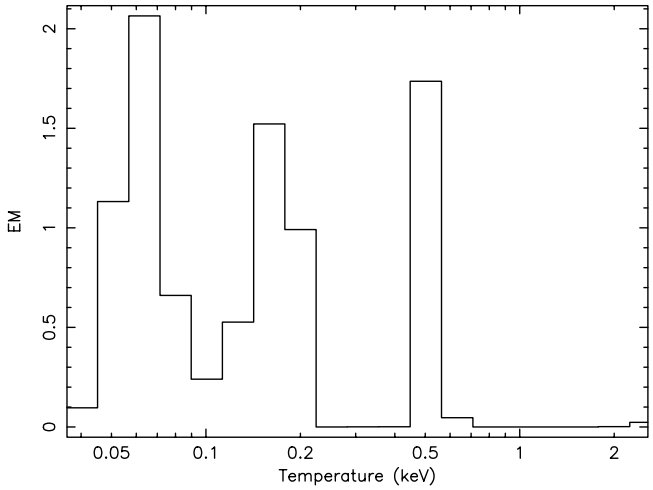

Fig. 4. DEM modeling of the EPIC-MOS+PN and RGS spectra of β Cen by means of the pdem method (see text). The emission measure EM is presented per logarithmic temperature bin.

5. Emission line fluxes

In Table 3 the measured fluxes at Earth (not corrected for interstellar absorption) of a number of prominent lines are given. The fluxes of RGS1 and RGS2 and of MOS1 and MOS2 have been measured by folding a Gaussian through the instrumental Line Spread Function and fitting to the data. A powerlaw is added to describe the continuum. Within parentheses the 1σ errors are given. For EPIC-MOS the resolution is too low to add statistical errors to the given wavelengths. The first three columns show the ion, the theoretical (laboratory) energy, and the theoretical wavelength, respectively. The other columns contain measured quantities of the observed features. The observed wavelengths are close to the theoretical values. No systematic red- or blueshift is noticed. This implies a low velocity plasma. Also tabulated are the $FWHM$ (in 0.001 keV) of the lines and the values relative to the energy E_0 of the lines. The measured broadenings are small. For most features only an upper limit could be determined. The value of 640 km s^{-1} given in Table 2 corresponds to a value of $FWHM/E_0 = 2\sqrt{\ln 2}v_{\rm mic}/c = 3.5$ (in units of 0.001). Some of the broadenings might be affected by blends. The O VIII line at 16.006 Å (as an example) might be blended by Fe XVIII.

5.1. Analysis of emission line profiles

5.1.1. Presence of asymmetric line profiles

Shapes of the X-ray lines have become an important diagnostic of the line formation processes. One of the first stars to be measured at high spectral resolution was the O4f star ζ Pup (Cassinelli et al. 2001). It showed very broad lines which are consistent with the lines being formed in a rapidly expanding wind, presumably, in shocks embedded in the wind. The lines of ζ Pup also were skewed with the shortward side being more prominant than the redward side. This general shape was predicted by MacFarlane et al. (1991). Profiles of this sort were also explained as arising in expanding winds by Ignace & Gayley (2002), and Kramer et al. (2003). One of the major surprises of recent X-ray observations is that ζ Pup appears to be unusual in showing the predicted profiles, because other massive stars have tended to show only the broadness but not the blueward skewness expected (Waldron et al. 2004).

Figure 5 shows the C VI line profile of β Cen together with a δ-function model. The latter is folded with the instrumental Line Spread Function. The top and middle panel of Fig. 5 shows the RGS2 and RGS1 spectrum respectively. In these panels the δ-function is centered around the top of the line feature. From both panels it is clear that the line is broader than the folded δ-function. In the bottom panel the RGS1 spectrum is shown again. However, the model is shifted such a way that it describes the blue wing of the feature, proving the asymmetry of the C VI line in the RGS1 spectrum. The asymmetry, however, is not confirmed in the RGS2 spectrum. Here only a broadening is noticed. The observed line broadening is only 1.4 times the instrumental line width. When interpreting the line profile asymmetry of the C VI line in the RGS1 spectrum, two caveats should be borne in mind: the line centroid shift is not large compared to the instrumental line width, and the line asymmetry is not clearly apparent in the RGS2 spectrum. Also note that identical δ-function model shapes were used for the bottom two panels of Fig. 5. In the bottom panel the model has simply been slightly shifted toward the short wavelength side. What appears to be a difference in shape between the bottom two convolved model profiles is simply an artifact of shifting the model by a non-integral number of bins.

5.2. He-like line diagnostics

Gabriel & Jordan (1969) were the first to demonstrate that forbidden (f), intercombination (i) and resonance (r) lines of the He-like "complex" provide useful diagnostics for X-ray emitting plasmas. More recent studies including the effects of dielectronic satellite lines and a radiation field have been carried out by Porquet et al. (2001). The ratio f/i is dependent on electron density because of the depopulation of the upper level of the f line at increasing density and can be used to derive electron densities in circumstances where radiation fields are relatively weak, such as in cool stars. However, in OB stars where the radiation fields are much stronger the depopulation of the upper level of the forbidden line occurs by radiative absorption (e.g., Blumenthal et al. 1972; Porquet et al. 2001) and the f/i ratio no longer indicates the density, but instead provides information on the mean intensity of the radiation field, hence the radial distance R of the X-ray source from the star (Waldron & Cassinelli 2001).

The fact that the UV radiation field is the dominant effect in determining the fir line strengths in β Cen is confirmed by detailed calculations. Using the formalism developed by Blumenthal et al. (1972), we calculate the radial dependence of R in the envelope of β Cen on the basis of a photospheric UV flux model for of Kurucz with $T_{\rm eff}$ = 21 100 K, $\log g$ = 4.0, and solar metallicity.

Table 3. Line fluxes at Earth of β Cen measured with EPIC-MOS and RGS. Statistical 1σ errors in the last digits in parentheses.

ion	E_0^a [keV]	λ_0^a [Å]	$\lambda_{\rm obs}^b$ [Å]	flux [10^{-13} erg cm^{-2} s^{-1}]	$FWHM^c$	$\frac{FWHM}{E_0}{}^d$	$\lambda_{\rm obs}{}^b$ [Å]	flux [10^{-13} erg cm^{-2}s^{-1}]	$FWHM^c$	$\frac{FWHM}{E_0}{}^d$
			MOS1					MOS2		
EPIC-MOS:										
S XV	2.461	5.039	4.979(.054)	0.04(.03)	–	–	4.979	0.01(.02)	–	–
Si XIII	1.853[e]	6.692[e]	6.692[f]	0.17(.03)	–	–	6.694(.046)	0.19(.04)	–	–
Mg XII	1.472	8.421	8.421[f]	0.11(.03)	–	–	8.421[f]	0.09(.02)	–	–
Mg XI	1.348[e]	9.200[e]	9.200[f]	0.34(.03)	–	–	9.200[f]	0.33(.03)	–	–
			RGS1					RGS2		
RGS:										
Mg XI	1.348[e]	9.200[e]	9.240(.064)	0.32(.15)	–	–	9.255(.048)	0.22(.13)	–	–
Ne X	1.2074	10.240	10.269(.—)	0.08($\lesssim$.22)	–	–	10.304(.028)	0.25(.10)	–	–
Ne X	1.0220	12.134	gap	–	–	–	12.142(.009)	0.57(.10)	–	–
Ne IX	0.9220	13.447	gap	–	–	–	13.447(.009)	0.70(.11)	2.9(2.4)	3.1
	0.9148	13.553	gap	–	–	–	13.554(.014)	0.52(.12)	2.9(2.4)	3.2
	0.9050	13.700	gap	–	–	–	13.751(.—)	0.06($\lesssim$.14)	2.9(2.4)	3.2
Fe XVII	0.8962	13.834	13.784(.018)	0.21(.09)	–	–	13.851(.009)	0.22(.07)	2.9(2.4)	3.2
	0.8925	13.892								
Ni XIX?	0.8830	14.040	–	–	–	–	14.045(.—)	0.08(.07)	–	–
Fe XVIII	0.8730	14.202	14.218(.009)	0.37(.09)	–	–	14.210(.014)	0.30(.08)	–	–
	0.8724	14.212								
Fe XVIII	0.8633	14.361	–	–	–	–	14.347(.023)	0.14(.07	–	–
	0.8626	14.373								
Fe XVIII	0.8529	14.536	14.538(.018)	0.16(.07)	–	–	–	–	–	–
Fe XVIII	0.8503	14.581	14.640(.032)	0.16(.07)	–	–	14.584(.019)	0.19(.07)	–	–
	0.8486	14.610								
Fe XVII	0.8258	15.013	15.014(.005)	1.28(.12)	$\lesssim$1.4	$\lesssim$1.7	15.019(.005)	1.17(.12)	$\lesssim$2.6	$\lesssim$3.2
O VIII	0.8170	15.176	15.167(.016)	0.27(.10)	$\lesssim$1.4	$\lesssim$1.7	15.151(.021)	0.28(.09)	$\lesssim$2.6	$\lesssim$3.2
Fe XVII	0.8125	15.260	15.255(.013)	0.51(.13)	$\lesssim$1.4	$\lesssim$1.7	15.258(.012)	0.48(.10)	$\lesssim$2.6	$\lesssim$3.2
O VIII	0.7745	16.006	16.012(.014)	0.48(.12)	4.2(2.1)	5.4	16.018(.011)	0.46(.08)	$\lesssim$4.8	$\lesssim$6.2
Fe XVII	0.7391	16.775	16.771(.005)	0.59(.09)	0.0	0.0	16.781(.009)	0.64(.11)	$\lesssim$2.0	$\lesssim$2.7
Fe XVII	0.7272	17.051	17.029(.009)	0.58(.13)	0.0	0.0	17.050(.026)	0.43(.38)	$\lesssim$2.0	$\lesssim$2.7
Fe XVII	0.7250	17.100	17.100[d]	1.30(.40)	0.0	0.0	17.096(.014)	1.08(.40)	$\lesssim$2.0	$\lesssim$2.7
O VII	0.6656	18.627	18.636(.011)	0.30(.07)	0.0	0.0	18.629(.016)	0.25(.08)	$\lesssim$4.1	$\lesssim$6.1
O VIII	0.6536	18.969	18.969(.003)	2.48(.14)	$\lesssim$0.6	$\lesssim$1.0	18.973(.003)	2.49(.14)	1.0(0.6)	1.5
O VII	0.5740	21.602	21.604(.003)	2.33(.14)	0.9(0.4)	1.6	gap	–	–	–
O VII	0.5686	21.804	21.798(.003)	1.98(.14)	1.0(0.4)	1.8	gap	–	–	–
O VII	0.5610	22.101	22.088(.—)	0.03($\lesssim$.09)	0.0	0.0	gap	–	–	–
N VII	0.5003	24.781	24.787(.021)	0.28(.11)	0.0	0.0	24.781(.010)	0.33(.07)	$\lesssim$1.9	$\lesssim$3.9
C VI	0.4356	28.466	28.451(.023)	0.19(.07)	1.2(1.2)	2.8	28.467(.023)	0.16(.06)	$\lesssim$1.9	$\lesssim$4.3
N VI	0.4307	28.787	28.764(.018)	0.15(.06)	–	–	28.812(.014)	0.24(.06)	$\lesssim$1.4	$\lesssim$3.3
N VI	0.4263	29.084	29.057(.035)	0.44(.14)	3.0(1.3)	7.1	29.093(.032)	0.15(.07)	$\lesssim$2.7	$\lesssim$6.4
N VI	0.4198	29.534	–	$\lesssim$0.04	–	–	–	–	–	–
Ca XIII?	0.4153	29.850	29.899(.024)	0.06(.04)	–	–	–	–	–	–
Ca XI?	0.4072	30.448	30.452(.024)	0.09(.05)	–	–	30.433(.083)	0.08(.06)	–	–
C VI	0.3675	33.736	33.736(.008)	1.13(.14)	0.9(0.2)	2.5	33.744(.006)	0.96(.10)	0.7(0.3)	2.0

Notes:

[a] E_0 and λ_0 are the theoretical energy and wavelength from Kelly (1987) and Dere et al. (2001).

[b] $\lambda_{\rm obs}$ is the observed wavelength with the statistical 1σ error in parentheses.

[c] $FWHM$ in 0.001 keV.

[d] in units of 0.001. For example, as $FWHM/E_0 = 2\sqrt{\ln 2}v_{\rm mic}/c = 1.665\ v_{\rm mic}/c$, a velocity $v_{\rm mic} = 300$ km s^{-1} corresponds to a broadening of $FWHM/E_0 = 1.665$ (cf. Tables 2).

[e] Theoretical value, as average of multiplet lines.

[f] Fixed to theoretical value.

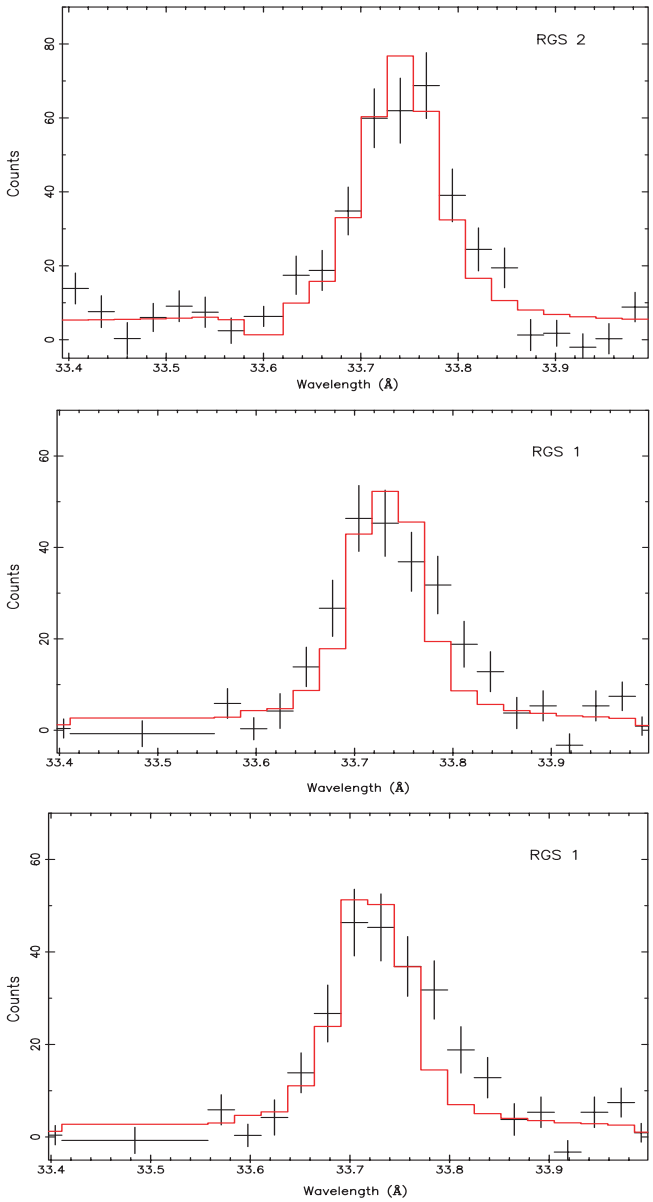

Fig. 5. C VI line in the RGS spectrum fitted by one δ-function folded with the instrumental line profile. From top to bottom RGS2, RGS1 (both with a centralized model), and RGS1 (with a shifted model). The profiles in all three panels are broader than the model. In the bottom panel (RGS1) the profile of the C VI line is slightly asymmetric which can be explained by models (see text).

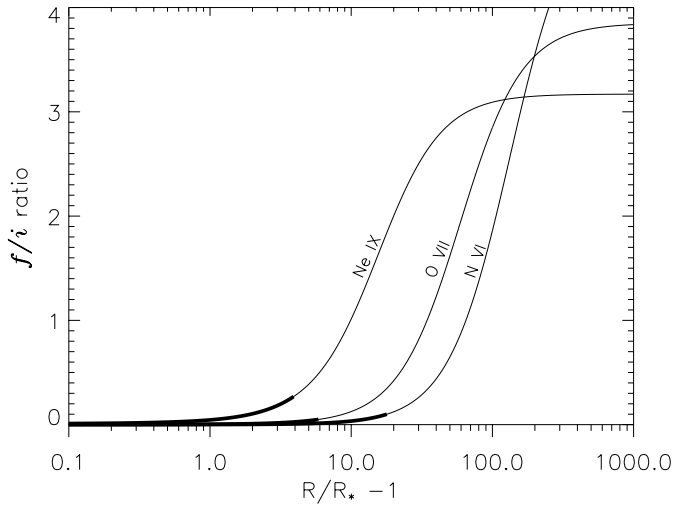

Fig. 6. The curves show the expected f/i line ratio as a function of formation radius R for the labeled He-like ions. The bold part indicates the distance from the stellar surface where the ion is located, based on the measured f/i ratios.

The mean intensity of the UV radiation is large near the surface of the star and it decreases outwardly by dilution factor

$$W(R) = \frac{1}{2}\left[1 - \left(1 - \left(\frac{R_*}{R}\right)^2\right)^{1/2}\right] \quad (1)$$

(Mewe & Schrijver 1978). As a result of the radial dependence of the radiation field, the observed f/i ratio can be used to derive the radial location of the He-like ions that are producing the observed fir lines. There are two He-like ions which allow reliable measurements of their f/i line ratio (O VII, Ne IX). These parameters indicate that the radiation field of β Cen will suppress the forbidden lines by radiative de-excitation of the upper level of f to much greater radii than would be possible with collisions (see, e.g., Waldron & Cassinelli 2001). Thus the expected f/i ratios as functions of radii for these ions are entirely controlled by the strength of the stellar UV radiation field. The predicted R dependencies of f/i are shown in Fig. 6. The f/i ratios derived from the RGS spectra for N VI, O VII, and Ne IX are: $\lesssim$0.1, $\lesssim$0.05, and $\lesssim$0.27, respectively (cf. Table 3). These results correspond to radial ranges R of the X-ray emission of about $\lesssim$17 R_*, $\lesssim$5.7 R_*, and $\lesssim$3.5 R_*, respectively. The higher ionized elements have upper limits for the radial ranges closer to the stellar surface.

Finally, using the results of Porquet et al. (2001) we extract from the measured $(i + f)/r$ ratios of 1.5, 0.86, and 0.83 (cf. Table 4) for N VI , O VII , and Ne IX electron temperatures of about $\lesssim$0.5, 2.3, and 3 MK, respectively, i.e., the temperatures of the regions from where we primarily observe the fir lines. The fact that Ne IX that is formed at about 0.3 keV is confined within about four stellar radii may imply that the hot plasma between about 0.3 and 0.6 keV (cf. Table 2) is confined by a strong magnetic field.

5.3. Temperature diagnostics

We carry out temperature diagnostics using temperature sensitive line ratios Ly_α/He_r. He_r stands for the resonance line of the line triplet in He-like ions. The ratios are calculated from the line fluxes as listed in Table 3. We assume plasma emissivities as calculated in the MEKAL code (Mewe et al. 1985), and compare measured ratios with the calculated emissivity ratios in order to derive line formation temperatures.

Mewe et al. (1985) calculates the X-ray line power, which is defined as $\mathcal{P} = -\log_{10}(P/n_e^2) - 23.0$ where n_e is the electron density in cgs units and P is power in cgs units, at different temperatures for various ions. From the difference of line powers we can calculate the ratio of line fluxes. The luminosity of

Table 4. The physical parameters for β Cen together with derived mass loss rates and terminal velocities. See text for details and references. The superscripts C and H refer to the cool and hot side of the bistability point, respectively.

$M/M_\odot$	Log $L/L_\odot$	$T_{\rm eff}$ (K)	$v_{\rm esc}$ (km s^{-1})	$\dot{M}^{\rm C}$ ($M_\odot$/yr)	$\dot{M}^{\rm H}$ ($M_\odot$/yr)	$v_\infty^{\rm C}$ (km s^{-1})	$v_\infty^{\rm H}$ (km s^{-1})
16	4.62	21100	642	1.25×10^{-7}	1.59×10^{-8}	835	1670

a given line can be written as, assuming the electron density is constant throughout the integrated volume

$$\begin{aligned} L &= \int P{\rm d}V \\ &= \int 10^{-(\mathcal{P}+23)}\, n_e^2 {\rm d}V \\ &= 10^{-23}\, n_{\rm e}^2 V \times 10^{-\mathcal{P}} \end{aligned} \quad (2)$$

then we can write the ratio of the fluxes as

$$\frac{f_1}{f_2} = \frac{L_1}{L_2} = 10^{\mathcal{P}_2-\mathcal{P}_1} \quad (3)$$

or

$$\log_{10}\frac{f_1}{f_2} = \mathcal{P}_2 - \mathcal{P}_1. \quad (4)$$

By taking the X-ray line powers for Ly$_\alpha$ and He$_r$ for each temperature that they have been calculated for, subtracting one from the other and comparing it to the line flux ratio we get a temperature estimate.

Although in the sensitivity range of RGS there are five such elements (Si, Mg, Ne, O and N) that would produce the required lines (*fir* triplet, Ly$_\alpha$) for this analysis, our observation yielded only two Ly$_\alpha$/He$_r$ pairs. Both the O VIII /O VII and N VII /N VI yielded the same temperature range of 2−2.5 MK.

6. Discussion

As described above we were not able to find firm X-ray variability on the time scale associated with the pulsations of β Cen. The EUVE observations of Cassinelli et al. (1996), and Cohen et al. (1996) of the β Cephei star β CMa gave strong indication that the pulsations at least have an effect on the upper regions of the photosphere where the Lyman continuum forms. It corresponds to a variation in the temperature of about 100 K. This seems small but the EUVE is formed well out in the Wien portion of a B star's continuum so even small temperature changes lead to exagerated variations. We considered it plausible at least that the pulsations could also affect the even higher regions in the atmosphere where wind shocks might originate. Our failure to find the expected correlation may mean that the processes by which line driven instabilities form and grow into shocks is more complicated than a 1D spherical model would predict.

It is well known that there can be a more circuitous route to the formation of wind shocks. For example for the Main sequence B star τ Sco (B0.5 V), Howk et al. (2000) were able to show that the anomalously hard X-rays and the absorption by O VI that extends to the red side of line center, can be explained by clumps that form in the wind. The picture that clumps form stall in their outward motion and fall back in toward the star is at least consistent with both *XMM* (Mewe et al. 2003) and *Chandra* (Cohen et al. 2003) observations of τ Sco.

Although it is not likely that we could derive such a complicated picture for the X-ray sources in β Cen, we have chosen to analyze the data sufficiently to uncover anomalies that might lead to a better understanding of this star. First we analyze a straightforward wind shock formation model for β Cen. This star is particularly interesting in that it lies very close to the bistability limit for luminous stars near B1 III to I (Vink et al. 2000). So we consider the possibility that the star lies on either side of the bistability jump. Also we consider the possible effects of wind wind collisions with the binary companion.

6.1. The Locations of the 3 X-ray components

One of our more firm conclusions is that there are three dominant temperatures that characterize the X-ray emission from β Cen, which we will call the soft medium and hard components, which are given in Table 1 and shown in Fig. 7.

Assuming that the X-rays are formed in shocks embedded in the stellar wind (Owocki et al. 1988) we can deduce the nature of these shocks from wind models. Typical shock models (e.g. Cooper & Owocki 1994) have jumps of about half the local wind speed. To get the temperature of the shocked material from the shock velocity jump Δv we can use the expression

$$T = \frac{3}{16}\frac{\mu m_{\rm H}\Delta v^2}{k} = 1.4\times10^7\ {\rm K}\left(\frac{\Delta v}{1000\ {\rm km\ s^{-1}}}\right)^2, \quad (5)$$

where $\mu m_{\rm H}$ is the average mass per particle. Also we can estimate the *EM* over a shock cooling length from the integral

$$EM = \int_{r_s}^{r_{s+l}} (\rho(r)/\mu m_{\rm H})^2 4\pi r^2 {\rm d}r \quad (6)$$

where r_s is the distance to the shock from the star and l is the cooling length. If one uses the expression $\dot{M} = 4\pi r^2\rho(r)v(r)$, and also assumes the standard beta velocity law $v(r) = v_\infty\left(1-\frac{R_*}{r}\right)^\beta$, where R_* is the radius of the star and v_∞ is the terminal wind velocity, the integral in Eq. (6) can be written as

$$EM = \frac{1}{4\pi}\left(\frac{\dot{M}}{\bar{m}v_\infty}\right)^2 \int_{r_s}^{r_{s+l}} {\rm d}r r^{-2}\left(1-\frac{R_*}{r}\right)^{-2\beta}. \quad (7)$$

We can get the cooling length using the MEKAL radiative energy loss curve and the first law of thermodynamics (dU = dQ − pdV, where $U = 3kT/2\bar{m}$, which provides $l = T({\rm d}T/{\rm d}r)^{-1}$). For the mass loss rate ($\dot{M}$) we used the

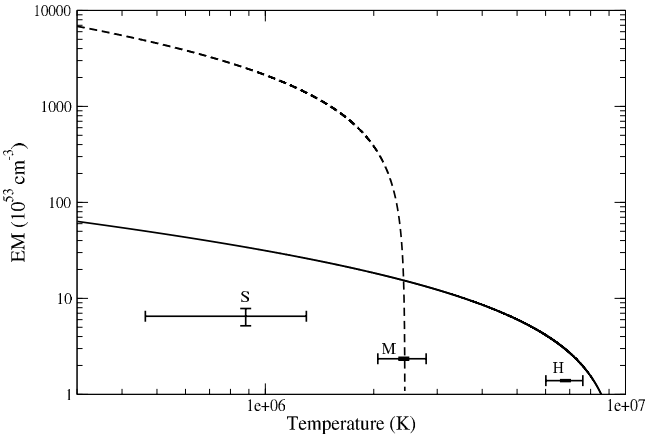

Fig. 7. Emission measure versus temperature, for a spherically symmetric shock. The *dashed* line is for the slower (cold side), the *solid* line is for the faster (hot side) wind. Also the *EM* and temperature of the soft (S), medium (M) and hard (H) components of the fit are shown. The error bars are 1σ errors associated with the fit.

results of the bistabiliy simulations of Vink et al. (2000). These simulations use a Monte Carlo code that followed the photons (emitted across the spectrum) which enter the wind. This model also accounts for the momentum deposition along with an accurate model of the wind and line opacities as obtained from non-LTE combined wind atmosphere code of de Koter et al. (1997). In their paper they give an analytic expression for the mass loss rate that is obtained from fitting the data. Interestingly, the temperature of β Cen is right at the jump temperature. Thus it is useful to compare results using parameters for either side and see if there is one that is a preferred explanation for our X-ray observations. The parameters are given in Table 4. Superscripts "H" and "C" refer to the hot and cool side of the bistability point. We used the results given in Fig. 2 of Vink et al. (2000), to obtain the mass loss rate instead of their fitting formulae. This was done to avoid the large errors associated with the extrapolation of the analytical expression to either side of the B1 spectral class.

We took the values for Log $L/L_\odot = 4.62$, $M/M_\odot = 16$ from Prinja (1989) together with the mass loss rates and terminal velocities to numerically find the dependence of *EM* on T (see Fig. 7).

Several results can be seen in Fig. 7. For the soft and medium bands the predicted emission measures are well above the observations. Based on similar model/observation comparisons for τ Sco, one can explain the differences by using the fact that the spherical shock picture overestimates the Emission measure in actual winds. As explained in Howk et al. (2000) the shocks are not likely to be spherical shells but rather in the form of shock fragments. Probably owing to instabilities such as Rayleigh Taylor because a fast low density wind is driving a much denser and slower high density spherical shell. If we allow for the likely possibility that the wind shocks are fragmentary, then one can explain the soft and medium results in Fig. 7 which correspond to the two temperatures (9.4×10^5 K and 2.4×10^6 K) in β Cen, we get the required *EM* for the soft component if 0.1–0.4% is shocked, but for the medium component from 1 to above 100% is needed. The model in Howk et al. (2000) also predicts that only ~1 percent of the wind needs to be shocked in order to generate the required luminosity. Our results for the soft and medium component seem to agree within the boundaries of uncertainties.

However, a problem is seen in regards to the hard component with the temperature (6.8×10^6 K). The hard component cannot be fit for the model in which we assumed the star to be on the cold side of the bistability limit. The primary reason for this is that the terminal velocity for a star on the cold side of the limit is simply not high enough to produce such hot shocks.

If on the other hand we assume that the star is on the hot side of the bistability limit, we see in Fig. 7 that a wind shock picture could explain all three temperature components, but in this case the fraction of the wind that is in the shock fragments is about 10%, a much larger fraction than in the model for the cool side of the bistability limit.

It is tempting at this point to conclude that the results established from the X-ray spectra indicate that β Cen is on the hot side of the bi-stability limit. However, we need to investigate whether it is possible that the hard X-rays arise from something other than shocks embedded in the wind.

6.2. Binarity of β Cen

Another possibility for contributions to the hard X-ray component is that it is coming from the shock generated from the collision of the wind with that of its companion.

Shobbrook & Robertson (1968) found velocity variations with a short and a long period from radial velocity measurements. More recently it has been shown that these short and long periods are 0.157 (Sterken & Jerzykiewicz 1993) and 357 days (Ausseloos et al. 2002), respectively. From interferometric measurements Robertson et al. (1999) calculated the separation of the binary components to be 15.6 ± 2 mas for the epoch 1995.013. From this information we estimated the physical separation of the binary components for the epoch 2003.2 to be ~4 AU (6×10^{13} cm).

The collision of winds in early type binary systems can produce a substantial flux of X-rays as shown by Stevens et al. (1992). One can estimate the X-ray luminosity of colliding winds to be

$$L_{\rm X} = \frac{\Lambda(T)}{(4\pi\bar{m})^2} \dot{M}^2 v^{-2} D^{-1} \eta^2 (1 + \eta^{-1/2}), \qquad (8)$$

where D is the distance between stars at the time of observation, Λ is the emissivity, $\dot{M}$ is the mass loss rate, v is the wind speed and η is the ratio of the wind ram pressure, which can be written as

$$\eta = \frac{\dot{M}_2 v_2}{\dot{M}_1 v_1}.$$

In the following we use for the cooling function, the expression $\Lambda = 1.64 \times 10^{-19} T^{-\frac{1}{2}}$ erg cm^3 s^{-1} as has been used by Feldmeier et al. (1997). Substituting this into Eq. (8) together with all the constants (in cgs units) we find

$$L_{\rm X} = 2.82 \times 10^{31} \dot{M}^2 v_\infty^{-3} D^{-1} \eta^2 (1 + \eta^{-1/2}) \text{ erg s}^{-1}. \qquad (9)$$

From Table 4 we can substitute the values for $\dot{M}$, v_∞ for the low speed wind and the distance D to get

$$L_X = 5.07 \times 10^{31}\, \eta^2 (1 + \eta^{-1/2})\ \mathrm{erg\,s^{-1}}. \quad (10)$$

From this we conclude that one needs $\eta \sim 0.15$ in order to be able to explain the hard component of the fit, for the case of a star on the cool side of the bistabilty limit. Although we find that the colliding winds generate enough *EM*, we also need to see if the temperature is sufficient. Luo et al. (1990) studied the two interesting cases: a) colliding equal winds with ($\eta = 1$) and b) the primary wind overwhelms the other ($\eta \sim 0$). For both cases they calculate the emerging spectrum of the colliding winds. The spectra peak at a certain energy ($kT_{\rm peak}$), which can be compared to the maximum temperature ($T_{\rm max}$). The region that has the highest temperature is where the wind comes to a dead stop. This can be obtained from Eq. (5) for the case where Δv is equal to the total wind speed. For β Cen this temperature is $T_{\rm max} = 1.0 \times 10^7$ K. From Figs. 7 and 8 of Luo et al. (1990) we calculated that $T_{\rm peak}/T_{\rm max} \sim 0.8$ for $\eta = 1$ and ~0.4 for $\eta \sim 0$, respectively. For the hard component $T_{\rm peak}/T_{\rm max} = 0.48$ which corresponds to $\eta \sim 0.2$, assuming a linear relation between $T_{\rm peak}$ and η. This value for η is very close to the one we obtained from the observed X-ray flux.

Thus to obtain a fit to the data for the slow wind case (i.e., the star being on the cool side of the bi-stability limit), we would need the hard X-rays to come from the interaction of the binary components. Then we also expect a different column density associated with this component. To check this we first split out the different temperature components. When we analyzed the individual components we saw that the medium and the hard components dominated the spectrum. For the hard component we allowed the column density ($N_{\rm H}$) to be different from the others. We used a series of column densities for the hard component ranging from (1 to 17) $\times 10^{19}$ cm^{-2}, while fitting the other parameters as described in Sect. 4. This procedure, which is effectively the addition of an extra parameter, did not improve the $\chi^2_{\rm red}$ of the fit.

In summary, the three X-ray temperature components can be explained in two ways. The star is on the hot side of the B1 bi-stability limit and has a wind fast enough to explain all three components as arising from fragmentary shocks in the wind. Alternatively the star could be on the cool side of the bi-stability limit and have a slower wind, but in this case the hard X-ray component would need to come from the colliding wind shock.

As a test to the explanations for the hard component one needs to observe β Cen at different epochs. We would expect variability in the hard component with a period of about 1 yr if the colliding winds scenario is responsible for the hard X-rays. Since the binary orbit is highly eccentric (~0.8, Ausseloos et al. 2002) and the luminosity is inversely proportional to the distance between the stars, we would expect an order of magnitude change in the luminosity. This would be easily observable if this is the case.

Acknowledgements. This paper is dedicated to the memory of co-author Rolf Mewe who died unexpectedly on May 4, 2004. J.P.C. is particularly grateful to Rolf for introducing him to the field of X-ray stellar astronomy in 1975, and for the long carreer in the field that has followed. This work is based on observations obtained with *XMM-Newton*, an ESA science mission with instruments and contributions directly funded by ESA Member States and the USA (NASA). J.P.C. and N.A.M. acknowledge support from NASA grants NAG5 5-9226 and GO2-3028, respectively. The SRON National Institute for Space Research is supported financially by NWO. We thank the referee for his fruitful comments

References

Agrawal, P. C., Singh, K. P., Riegler, G. R., & Stern, R. A. 1984, MNRAS, 208, 845
Anders, E., & Grevesse, N. 1989, Geochim. Cosmochim. Acta, 53, 197
Audard, M., Güdel, M., Sres, A., et al. 2003, A&A, 398, 1137
Ausseloos, M., Aerts, C., Uytterhoeven, K., et al. 2002, A&A, 384, 209
Blumenthal, G. R., Drake, G. W. F., & Tucker, W. H. 1972, ApJ, 172, 205
Breger, M. 1967, MNRAS, 136, 51
Cassinelli, J. P., Cohen, D. H., & MacFarlane, J. J. 1994, ApJ, 421, 705
Cassinelli, J. P., Cohen, D. H., & MacFarlane, J. J., et al. 1996, ApJ, 460, 949
Cassinelli, J. P., Miller, N. A., Waldron, W. L., MacFarlane, J. J., & Cohen, D. H. 2001, ApJ, 554, L55
Cohen, D. H., MacFarlane, J. J., & Cassinelli, J. P. 1996, Astrophysics in the extreme ultraviolet, Proc. coll. No. 152 International Astronomical Union; held in Berkeley; California; March 27–30; 1995 (Dordrecht: Kluwer Academic Publ.), ed. S. Bowyer, & R. F. Malina, 389
Cohen, D. H., de Messières, G. E., MacFarlane, J. J., et al. 2003, ApJ, 586, 495
Cooper, R. G., & Owocki, S. P. 1994, Ap&SS, 221, 427
den Herder, J. W., Brinkman, A. C., & Kahn, S. M., et al. 2001, A&A, 365, L7
Dere, K. P., Landi, E., Young, P. R., & Del Zanna, G. 2001, ApJS, 134, 331
Feldman, U. 1992, Phys. Scr., 46, 202
Feldmeier, A., Kudritzki, R. P., Palsa, R., et al. 1997, A&A, 320, 899
Flower, P. J. 1977, A&A, 54, 31
Fruscione, A., Hawkins, I., Jelinsky, P., & Wiercigroch, A. 1994, ApJS, 94, 127
Gabriel, A. H., & Jordan, C. 1969, MNRAS, 145, 241
Grevesse, N., & Sauval, A. J. 1998, in Solar Composition and its Evolution – From Core to Corona, ed. C. Frölich, M. C. E. Huber, S. K. Solanki, & R. von Steiger, Space Sci. Rev., 85, 161
Grevesse, N., & Sauval, A. J. 1999, A&A, 347, 348
Grillo, F., Sciortino, S., Micela, G., Vaiana, G. S., & Harnden, F. R., Jr. 1992, ApJS, 81, 795
Howk, J. C., Cassinelli, J. P., Bjorkman, J. E., & Lamers, H. J. G. L. M. 2000, ApJ, 568, 954
Ignace, R., & Gayley, K. G. 2002, ApJ, 534, 348
Jansen, F., Lumb, D. H., & Altieri, B., et al. 2001, A&A, 365, L1
Kaastra, J. S., Mewe, R., & Nieuwenhuijzen, H. 1996a, in UV and X-ray Spectroscopy of Astrophysical and Laboratory Plasmas, ed. K. Yamashita, & T. Watanabe (Tokyo: Universal Academy Press, Inc.), 411 (SPEX)
Kaastra, J. S., Mewe, R., Liedahl, D. A., et al. 1996b, A&A, 314, 5

Kaper, L. 1999, in Variable and Non-spherical Stellar Winds in Luminous Hot Stars, ed. B. Wolf, O. Stahl, & A. W. Fullerton, IAU Coll., No. 169
Kaper, L., Henrichs, H. F., Nichols, J. S., & Telting, J. H. 1999, A&A, 344, 231
Kelly, R. L. 1987, Atomic and Ionic Spectrum lines below 2000 Angstroms: Hydrogen through Krypton, J. Phys. Chem. Ref. Data, 16, Suppl. 1
de Koter, A., Heap, S. R., & Hubeny, I. 1997, ApJ, 477, 792
Kramer, R. H., Cohen, D. H., & Owocki, S. P. 2003, A&A, 592, 532
Lesh, J. R., & Aizenman, M. L. 1978, ARA&A, 16, 215
Luo, D., McCray, R., & Mac Low, M.-M. 1990, ApJ, 362, 267
MacFarlane, J. J., Cassinelli, J. P., Welsh, B. Y., et al. 1991, ApJ, 380, 564
Mewe, R., Gronenschild, E. H. B. M., & van den Oord, G. H. J. 1985, A&AS, 62, 1 (MEKAL)
Mewe, R., Kaastra, J. S., & Liedahl, D. A. 1995, Legacy, 6, 16 (MEKAL)
Mewe, R., Raassen, A. J. J., Cassinelli, J. P., et al. 2003, A&A, 398, 203
Mewe, R., & Schrijver, J. 1978, A&A, 65, 99
Owocki, S. P., Castor, J. I., & Rybicki, G. B. 1988, ApJ, 335, 914
Perryman, M. A. C., & the Hipparcos Science Team 1997, The Hipparcos and Tycho Catalogues (ESA report SP-1200; Noordwijk: ESA), A&A, 323, L49
Porquet, D., Mewe, R., Dubau, J., Raassen, A. J. J., & Kaastra, J. S. 2001, A&A, 376, 1113
Prinja, R. K. 1989, MNRAS, 241, 721
Raassen, A. J. J., Mewe, R., Audard, M., et al. 2003, A&A, 411, 587
Robertson, J. G., Bedding, T. R., & Aerts, C., et al. 1999, MNRAS, 302, 245
Shobbrook, R. R., & Robertson, J. W. 1968, Proc. Astro. Soc. Aust., 1, 82
Sterken, C., & Jerzykiewicz, M. 1993, Space Sci. Rev., 62, 95
Stevens, I. R., Blondin, J. M., & Pollock, A. M. T. 1992, ApJ, 386, 265
Strüder, L., Briel, U. G., Dennerl, K., et al. 2001, A&A, 365, L18
Turner, M. J. L., Abbey, A., Arnaud, M., et al. 2001, A&A, 365, L27
Vink, J. S., de Koter, A., & Lamers, H. J. G. L. M. 2000, A&A, 362, 295
Waldron, W. L., & Cassinelli, J. P. 2001, ApJ, 548, L45
Waldron, W. L., Cassinelli, J. P., Miller, N. A., MacFarlane, J. J., & Reiter, J. C. 2004, ApJ, 616, 542